ACS NANO

www.acsnano.org

ARTICLE

Wireless, Battery-Free Implants for Electrochemical Catecholamine Sensing and Optogenetic Stimulation

Tucker Stuart, William J. Jeang, Richard A. Slivicki, Bobbie J. Brown, Alex Burton, Victoria E. Brings, Lilian C. Alarcón-Segovia, Prophecy Agyare, Savanna Ruiz, Amanda Tyree, Lindsay Pruitt, Surabhi Madhvapathy, Martin Niemiec, James Zhuang, Siddharth Krishnan, Bryan A. Copits, John A. Rogers, Robert W. Gereau, IV, Vijay K. Samineni,* Amay J. Bandodkar,* and Philipp Gutruf*

Cite This: *ACS Nano* 2023, 17, 561−574

Read Online

ACCESS | Metrics & More | Article Recommendations | Supporting Information

ABSTRACT: Neurotransmitters and neuromodulators mediate communication between neurons and other cell types; knowledge of release dynamics is critical to understanding their physiological role in normal and pathological brain function. Investigation into transient neurotransmitter dynamics has largely been hindered due to electrical and material requirements for electrochemical stimulation and recording. Current systems require complex electronics for biasing and amplification and rely on materials that offer limited sensor selectivity and sensitivity. These restrictions result in bulky, tethered, or battery-powered systems impacting behavior and that require constant care of subjects. To overcome these challenges, we demonstrate a fully implantable, wireless, and battery-free platform that enables optogenetic stimulation and electrochemical recording of catecholamine dynamics in real time. The device is nearly 1/10th the size of previously reported examples and includes a probe that relies on a multilayer electrode architecture featuring a microscale light emitting diode (μ-LED) and a carbon nanotube (CNT)-based sensor with sensitivities among the highest recorded in the literature (1264.1 nA μM^{-1} cm^{-2}). High sensitivity of the probe combined with a center tapped antenna design enables the realization of miniaturized, low power circuits suitable for subdermal implantation even in small animal models such as mice. A series of *in vitro* and *in vivo* experiments highlight the sensitivity and selectivity of the platform and demonstrate its capabilities in freely moving, untethered subjects. Specifically, a demonstration of changes in dopamine concentration after optogenetic stimulation of the nucleus accumbens and real-time readout of dopamine levels after opioid and naloxone exposure in freely behaving subjects highlight the experimental paradigms enabled by the platform.

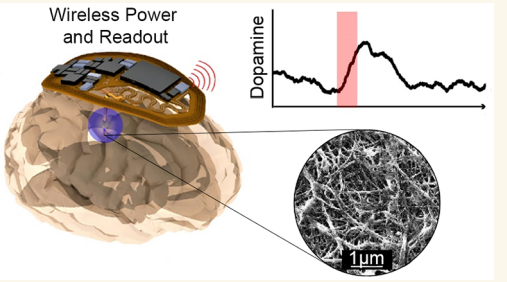

KEYWORDS: *wireless, battery-free, optogenetics, carbon nanotubes, catecholamine, dopamine*

INTRODUCTION

The progression of technology for monitoring neurological signals has substantially expanded the capabilities and understanding of neuroscience over the past decade.[1−4] Despite this, the available technologies for such studies largely require bulky, power intensive benchtop systems with complicated operational procedures that require highly trained staff and constant care of the experimental subjects. Real-time, continuous monitoring of *in vivo* neurotransmitter dynamics presents a key operational capability that is needed to fully elucidate neural pathways involved in several disease archetypes.[5,6] Of particular interest among neurotransmitters are catecholamines, particularly dopamine (DA), due to their role in behavioral factors such as motivation[7] and pleasure,[8,9] as well as disease archetypes such as addiction, Alzheimer's,[10−12] and Parkinson's disease.[13−16] The development of technologies to monitor dynamics of these neurotransmitters have largely focused on electrochemical sensing modalities, which are reliant on tethered sensing devices that adversely impact subject behavior and limit experimental paradigms.[17−20] Alternative strategies that rely on aptamer-based transistor sensors also face similar issues in addition to

Received: September 23, 2022
Accepted: December 16, 2022
Published: December 22, 2022

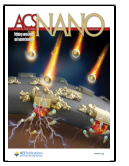

https://doi.org/10.1021/acsnano.2c09475
ACS Nano 2023, 17, 561−574

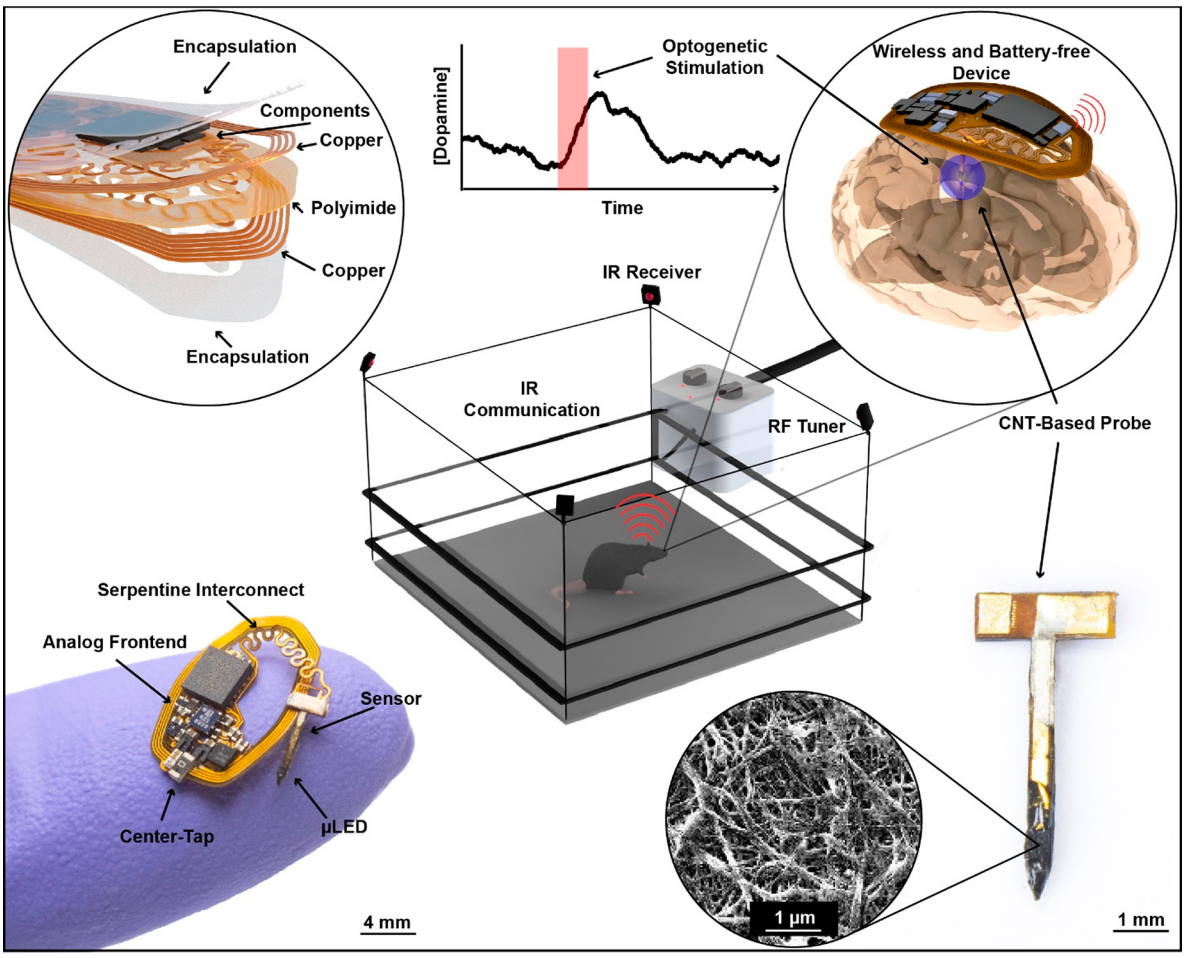

Figure 1. Platform Overview: Illustration showing operational principle of the subdermally implantable, wireless, and battery-free devices for long-term monitoring of catecholamine dynamics in the brain.

challenges associated with signal irreversibility, thus impeding acquisition of real-time transients.[21,22] The progression of electrochemical detection platforms supported by small, wireless device form factors seek to address these shortcomings through the elimination of tethered connections, allowing for freely moving subjects and reducing the impact on naturalistic behavior.[23,24] These devices, however, remain reliant on bulky, oversized batteries (>2 g),[24] which impede uninterrupted operation, increases subject handling requirements, impose operational burden, and negatively impact subject social behavior.[25] These factors are particularly limiting when correlating behavioral phenotype with biochemical measures of neural activity. Additionally, these drawbacks collectively limit the ability to perform reliable, high-throughput chronic studies.

The development of lightweight, fully implantable, wireless, and battery-free devices has previously been accomplished for optogenetics[26,27] and electrical stimulation.[28] Nonetheless, a battery-free device for capturing neurochemical dynamics using electrochemical sensors has not been demonstrated yet, because sensors require sophisticated electronic circuitry that can handle low current (nanoampere to picoampere) amplification and microvolt accurate biasing—features that cannot be easily offered in a battery-free format. Among these devices, even fewer host capabilities of simultaneous stimulation and recording.[25] Electrical stimulation protocols have been used for investigating DA in certain regions of the brain;[29−31] however, optogenetics offers a favorable alternative to electrical stimulation because of cell specificity and enhanced spatial resolution.[32−34] Optogenetics in combination with direct chemical recording also reduces stimulation artifacts particularly important for highly sensitive electrical recordings required for electrochemical sensors.[35] Simultaneous optogenetic stimulation and electrochemical recording of DA dynamics poses significant progression of device functionality for deciphering neural pathways associated with catecholamine-related disorders, as well as enabling experimental paradigms targeting specific neuronal populations to understand relationships between DA release and behavior.

In this work, we introduce a wireless and battery-free device capable of real-time, multimodal optogenetic stimulation and electrochemical recording of transient DA dynamics in the brain. The described system is nearly 10 times smaller than previously reported battery-powered systems and implements circuit designs needed for electrochemical sensing and amplification.[24,36] The miniaturization is achieved through three key aspects: (1) a catecholamine sensor composed of single walled carbon nanotubes (SWCNT)-carbon fiber (CF) composite electrodes that offer some of the highest sensitivities reported in the literature;[37−39] (2) wireless, battery-free electronic circuits that employ center-tapped antenna schemes with a double-sided antenna structure and magnetic resonant coupling (MRC) capabilities for robust powering of digital electronics and reference biasing without the need for bulky

https://doi.org/10.1021/acsnano.2c09475
ACS Nano 2023, 17, 561−574

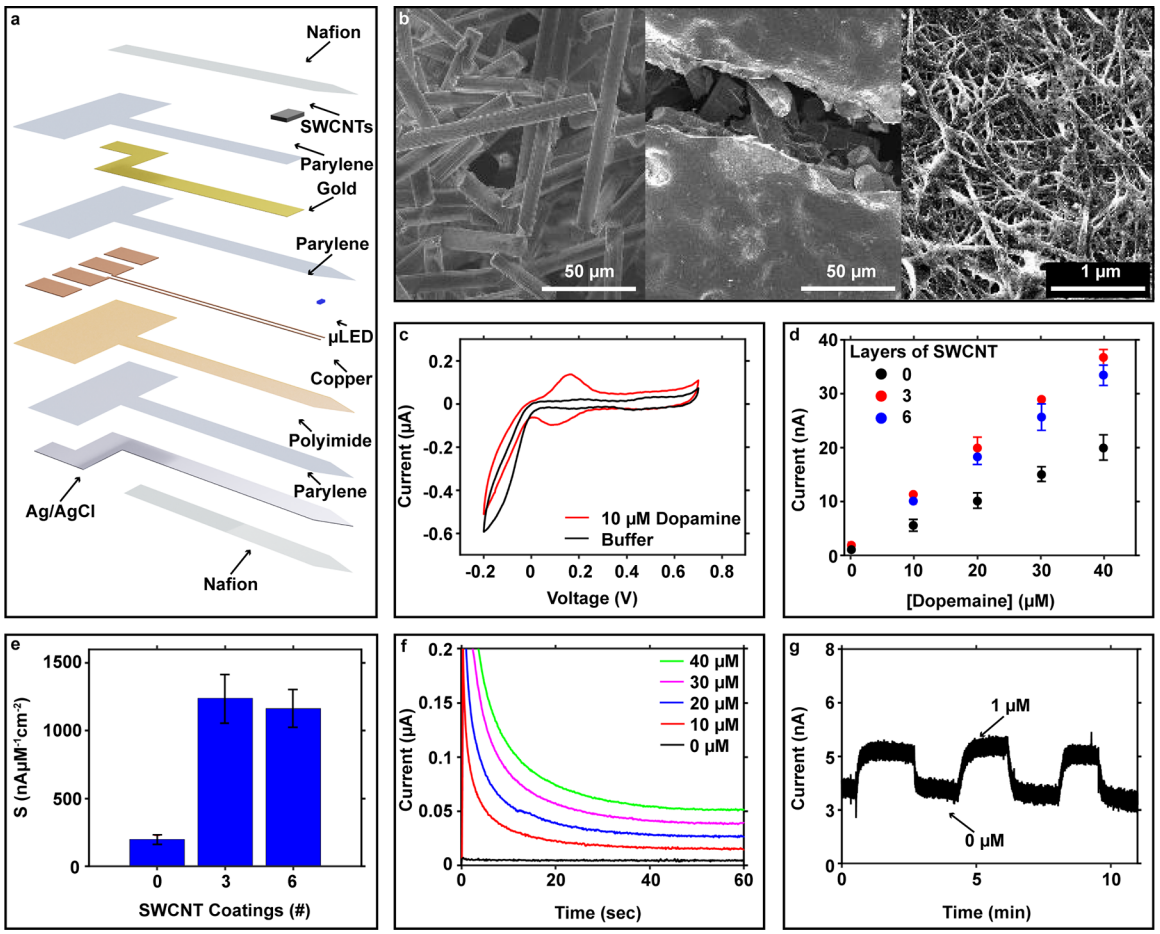

Figure 2. Probe Characterization: (a) Exploded schematic showing layer composition of microneedle structure. (b) Scanning electron microscopy (SEM) images of CF/chitosan composite (left), pyrolyzed CF/chitosan composite with a cracked region to reveal the interior CF support structure (center), and SWNCT-coated on CF/chitosan (SWNCT-CF) composite (right). (c) Cyclic voltammetry of the sensor (without the Nafion permselective membrane) in the absence and presence of dopamine. (d) Normalized calibration plot and (e) sensitivity for SWCNT-CF composite electrodes with varying layers of SWCNT coats. (f) Sensor response to increasing concentrations of dopamine (0−40 μM) (n = 3). (g) Transient sensor response and recovery to 1 μM dopamine solution.

potentiostats; and (3) a heterogeneous fabrication process combining laser patterning, lithography, and thin-film deposition that allows for seamless assembly of the SWCNT/CF composite electrodes on flexible electronics layouts. The resulting system achieves high fidelity recordings while maintaining a device form factor that is fully implantable and offers simultaneous stimulation and recording of DA dynamics in small animal models, which allow for long-term, ethologically relevant experimental designs, well beyond the capabilities of conventional stimulation and recording methods.

RESULTS AND DISCUSSIONS

Wireless, Battery-Free, and Fully Implantable Devices for Monitoring and Modulation of Dopamine Dynamics. Figure 1 provides an outline of how subdermal implanted multimodal devices enable real-time, continuous monitoring in a freely moving subject by utilizing wireless power transfer (WPT) technologies integrated into the animal housing. Devices comprise a monolithic multilayer laminate populated with commercially available surface mount components and features low-power-amplification circuits. For long-term device function, encapsulation and biocompatibility are essential factors to consider.[40,41] These devices are encapsulated in parylene C to provide a biofluid barrier and polydimethylsiloxane (PDMS) to match Young's modulus of the device surface to that of the surrounding tissue, thereby minimizing impact of the implantation procedure to surrounding tissue.[23,42−44] The device utilizes MRC at 13.56 MHz for WPT[3,23,25−28,45,46] and features a center-tapped antenna structure for the conversion of harvested alternating current (AC) to direct current (DC) with negative and positive potential for supplying reference voltages to the sensor and powering digital electronic components, respectively. To reduce device footprint, the antenna side supplying positive voltage for digital signal processing and communication circuits composed of six turns is placed on the backside of the device while the antenna side supplying negative voltage for biasing the electrochemical sensors is placed on the top side, allowing for dense population of active and passive electronic components (see Figure S1). Antenna sides are defined by a center tap with rectification and voltage regulation. This device architecture allows for wireless supply of both voltages without the use of many passive components, enabling a highly miniaturized device without the need for large, power hungry potentiostat integrated circuits (ICs) and yields a subdermmaly implantable format.

All electrical components used in the fabrication of the device feature ultrasmall rigid footprints to reduce device bulk

https://doi.org/10.1021/acsnano.2c09475
ACS Nano 2023, 17, 561−574

without sacrificing functionality (see Figure S2). The microcontroller (μC) controls μ-LED optogenetic stimulation using radio frequency (RF) amplitude shift keying and infrared (IR) data communication with a modulated carrier frequency of 57 kHz.[28] IR communication is selected due to the small hardware footprint needed for communication, with data rates that are suitable for long-term electrochemical recording (25 Hz) across the entire experimental arena (see Figure S3). The final device embodiment, shown in Figure 1, results in device dimensions of 12 mm × 8.5 mm × 3.2 mm and a total weight of less than 49 mg, substantially smaller and lighter, with less volume displacement than previously reported devices.[24,36]

A flexible serpentine structure (270 μm width) serves as a connection between the device body and the injectable stimulation and sensing probe, which enables articulation of the probe during implantation procedures without compromising electrical connectivity and structural stability.[47,48] Thin serpentine interconnects are chosen and designed to enable sustained, effective stretchability without surpassing yield strain in the copper layers of the device and allowing for motion artifact-free recording during *in vivo* operation (see Figure S4). The thin, flexible profile allows for conformal application to the skull with complete subdermal implantation, resulting in seamless device integration and improved subject recovery (see Figure 1). A custom animal enclosure for wireless, battery-free device operation is functionalized with a two-turn antenna with turns placed at heights of 3 and 6 cm, which correspond to heights of the subject during walking and rearing, respectively.[26] The resulting system enables continuous recording of DA dynamics in the brain with capabilities of optogenetic stimulation and simultaneous recording without impeding subject behavior or interactions with an operant.

Electrochemical Sensor Layout and Characterization. Functionality of the device is achieved through the deployment of a miniaturized neural probe (150 μm^2 cross sectional area) that integrates a μ-LED for optogenetic stimulation and a high sensitivity electrochemical sensor (see Figure 2a) for DA detection. The flexible probe is fabricated on a polyimide sheet with patterned copper traces for connecting a blue μ-LED followed by parylene encapsulation and deposition of a thin film of gold (thickness: 150 nm) on the top side, which acts as the current collector for the DA sensor. Another layer of parylene atop the Au layer defines the working electrode (WE) area to which the SWCNT-CF composite electrode is attached *via* carbon ink for electrochemical detection of DA. The back side of the probe is coated with silver/silver chloride ink, which serves as a combined counter and reference electrode. Finally, a layer of Nafion is coated over the SWCNT-CF and Ag/AgCl electrodes to impart selectivity to the WE by rejecting negatively charged electroactive species, such as uric acid and ascorbic acid, which are commonly found in cerebrospinal fluid and have similar oxidation potentials to that of DA.[49]

The selection of the SWCNT-CF composite electrode is based on our initial extensive screening of different materials for developing the WE including nano-/microporous metals and their alloys electrodeposited on planar gold-based WE. Panels a–c of Figure S5 illustrate the comparison of the response of these WEs for detecting DA. A follow-up investigation of carbonaceous materials reveals that a commercial CF sheet offers enhanced performance over our initial screen of metallic electrode materials with a sensitivity ~250 nA μM^{-1} cm^{-2} (Figure S5d). To further improve sensitivity, we synthesized a CF-polymer composite as an intermediate layer. This is achieved by first treating the commercial CF sheet with corona discharge to improve its hydrophilicity, followed by coating a suspension of milled CF in chitosan (see Figure 2b, left image). The CF/chitosan composite then undergoes a rapid thermal treatment to generate a conductive surface (see Figure 2b, center image) with an underlying commercial CF sheet for mechanical and electrical support. Serial dip-coating and film annealing of SWCNTs in Nafion solution (see Figure 2b, right image) enables dramatic enhancement in sensor sensitivity.

Figure 2c shows the cyclic voltammogram for the SWCNT-CF composite electrode in the absence and presence of dopamine, clearly illustrating the reversible oxidation and reduction of dopamine. Here, a conventional three-electrode system composed of the SWCNT-CF composite electrode as WE, liquid junction Ag/AgCl-based reference electrode (RE), and platinum-based counter electrode (CE) is used. The proximity and near equal heights of the redox peaks indicate that the developed electrode is ideal for sensing catecholamines. Parts d and e of Figure 2 exhibit the effect of number of layers of SWCNTs on sensor sensitivity, while Figure 2f illustrates the chronoamperometric response to increasing dopamine concentrations for a three-layer SWCNT-CF composite electrode. The results shown in Figure 2d–f are obtained using a two-electrode setup consisting of the SWCNT-CF composite electrode as WE and printed Ag/AgCl as combined RE/CE electrode. The results reveal that three layers of SWCNTs offers the best performance (sensitivity 1264.1 nA μM^{-1} cm^{-2}), which is among the highest reported in the literature (see Table S1).[37−39] It should also be noted that our probe detects catecholamine at +0.32 V (see Figure S6c), which is lower than most of the sensors reported earlier and is therefore less susceptible to interference. This reference voltage is set to the lowest bias voltage with sufficient sensitivity to detect micromolar changes in DA concentration (as seen in the amperometric data in Figure 2f). A mild decrease in sensitivity is recorded for electrodes coated with six layers of SWCNTs. This may be attributed to reduced porosity and hence lower electroactive area occurring due to overcrowding of the SWCNTs onto the electrodes. Based on these results, a WE composed of three layers of SWCNTs is utilized for all future experiments.

A fast reversible response to changing neurotransmitter concentrations is crucial for capturing subtle neurotransmitter transients *in vivo*. The reversibility of the probe is investigated under *in vitro* conditions using a flow pump to pulse alternating solutions containing either 0 or 1 μM of DA at high flow rates (2 mL/min) to mimic rapid dopaminergic fluctuations experienced *in vivo* as reported earlier (see the Methods section).[50] As shown in Figure 2g, the probe shows excellent reversibility with minimal hysteresis, indicating its potential for real-time sensing in animals (see the Methods section). Figure S6 highlights the effectiveness of Nafion in imparting permselectivity for DA in the presence of uric and ascorbic acid, which are commonly present in cerebrospinal fluid at a high concentration and oxidize at similar potentials to DA.[51,52] Cyclic voltammetry measurements demonstrate the performance of the sensors with and without the coating upon subsequent addition of each interfering species at concentrations 50 times higher than that of DA. Uncoated sensors exhibit substantial increase in the oxidation and reduction peak amplitudes upon introduction of these interfering species. In contrast, coated sensors feature negligible increase in signal,

https://doi.org/10.1021/acsnano.2c09475
ACS Nano 2023, 17, 561−574

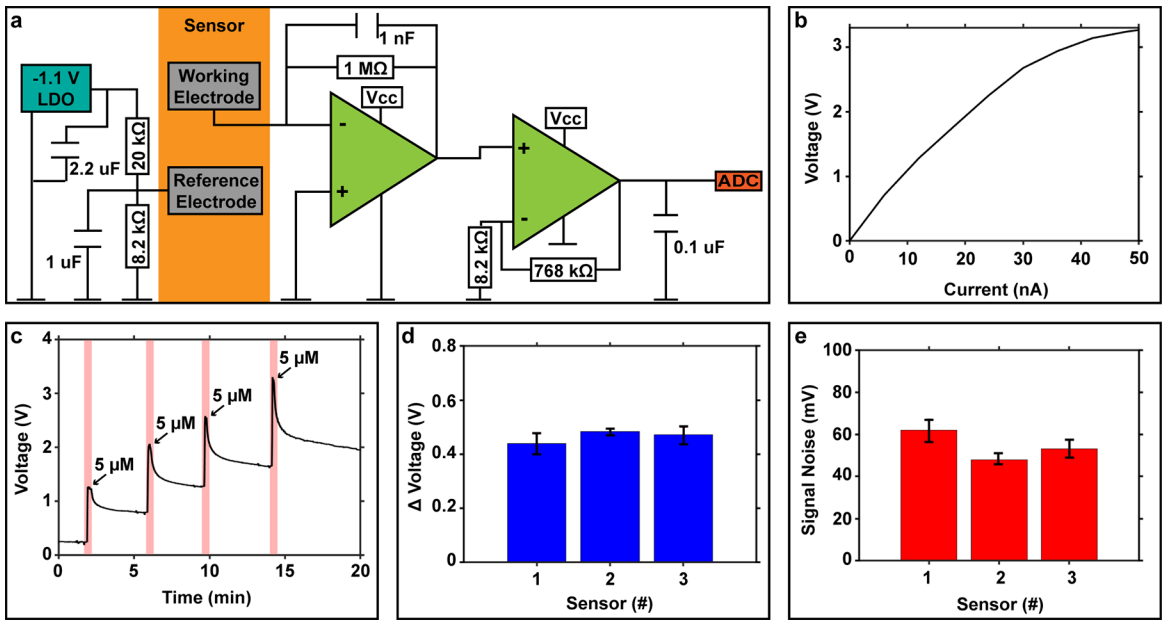

Figure 3. Analog Front End: (a) Electrical schematic showing analog front and reference electrode supply. (b) Wirelessly recorded output voltage with varying current inputs to analog front end circuit. (c) Wireless recording of increased dopamine concentration in solution with 5 μM spikes (red). (d) Wirelessly recorded voltage response for multiple sensors (n = 3) responding to 5 μM spikes in dopamine concertation. (e) Wirelessly recorded signal noise for multiple sensors (n = 3).

indicating the effectiveness of Nafion in minimizing the effect of uric acid and ascorbic acid on sensor performance. Results from additional experiments studying the effect of duration of corona treatment of pristine CF film-based electrodes to improve sensitivity (Figure S7a); the response of the SWCNT-CF composite electrode (with three layers of SWCNTs, *i.e.*, the final composition of the selected WE material) to 1 μM spikes of DA (Figure S7b) and its baseline (Figure S7c) and sensitivity (Figure S7d) stability appear in the Supporting Information.

Electrochemical Recording Electronics. Miniaturization of highly sensitive electrochemical bias generation and amplification of nanoampere currents is achieved through carefully tuned circuits with small package, off-the-shelf components. Electrochemical recordings of this nature are usually developed using a potentiostat IC or similar circuits,[24] which require extensive, complex circuitry and substantial passive components, compromising the ability to miniaturize the platform. Additionally, these circuits require significant power for operation (>4.85 mW),[53] limiting their use with wireless and battery-free device architectures. Reduction of component size, count, and power requirements is critical to meet footprint requirements while delivering performance suitable for high fidelity readouts. For the device shown here, functionality is achieved through implementation of analog circuity described in Figure 3a. Regulated negative voltage from the linear regulator is divided to produce the operational reference voltage for the detection of dopamine. A constant −0.32 V is applied to the RE (as obtained from the cyclic voltametric and chronoamperometric studies reported in Figure 2) and stabilized using a 1 μF capacitor. The current produced at the WE is measured using a transimpedance amplifier with 1 × 10^6 gain to convert 1 nA of signal to 1 mV. The resulting signal is then amplified through a noninverting amplifier with a fixed gain of 94.6. A passive lowpass filter is used to remove high-frequency noise from the signal before digital conversion by a 10-bit ADC oversampled to 12-bit. This analog front-end consumes an average of 201.8 μW.

The resulting signal output, shown in Figure 3b, demonstrates the analog front end response to currents between 0 and 50 nA, chosen based on results from Figure 2 and estimated physiological ranges. A linear response is observed between 0 and 30 nA of current, which then becomes nonlinear at higher current inputs, likely resulting from high gain distortion from the amplification stages. It is critical to note that the physiologically relevant range[54−56] overlaps with the linear range of the amplifier circuit and that nonlinearities of the amplifier circuit can be corrected *via* a lookup table in the microcontroller. To measure wireless and battery-free performance of the system, benchtop experiments were conducted as described in the Methods section. Figure 3c shows the resulting signal output from this experiment with stepwise DA concentration increases of 5 μM. With each increase in solution concentration, a spike in signal is observed, generating a peak signal increase of 1.30 V, which reaches steady state after 5 min of recording, resulting in an average signal change of 0.44 V from baseline after the addition of DA. The singal drift is characterized in Figure S7c, which is approximately 0.7 nA/h. For most neuroscience paradigms, this drift is acceptable as the focus is on signal change rather than absolute changes which vary substantially with physiology.[57−59] Inconsistencies arising from sensor manufacturing and component tolerance may cause variance among the realized sensitivity of the system. This work focuses on a two-electrode system to minimize sensor complexity and its sensitivity to drift future embodiments may mitigate this *via* three-electrode setups. Figure 3d shows the signal response for three different devices. An average sensitivity of 86 mV/μM with a standard deviation of 7.6 mV within the linear output range between 0 and 30 nA of estimated current output is observed. The measured noise of the system is plotted in Figure 3e, which shows a mean noise of 54.3 mV with a

https://doi.org/10.1021/acsnano.2c09475
ACS Nano 2023, 17, 561−574

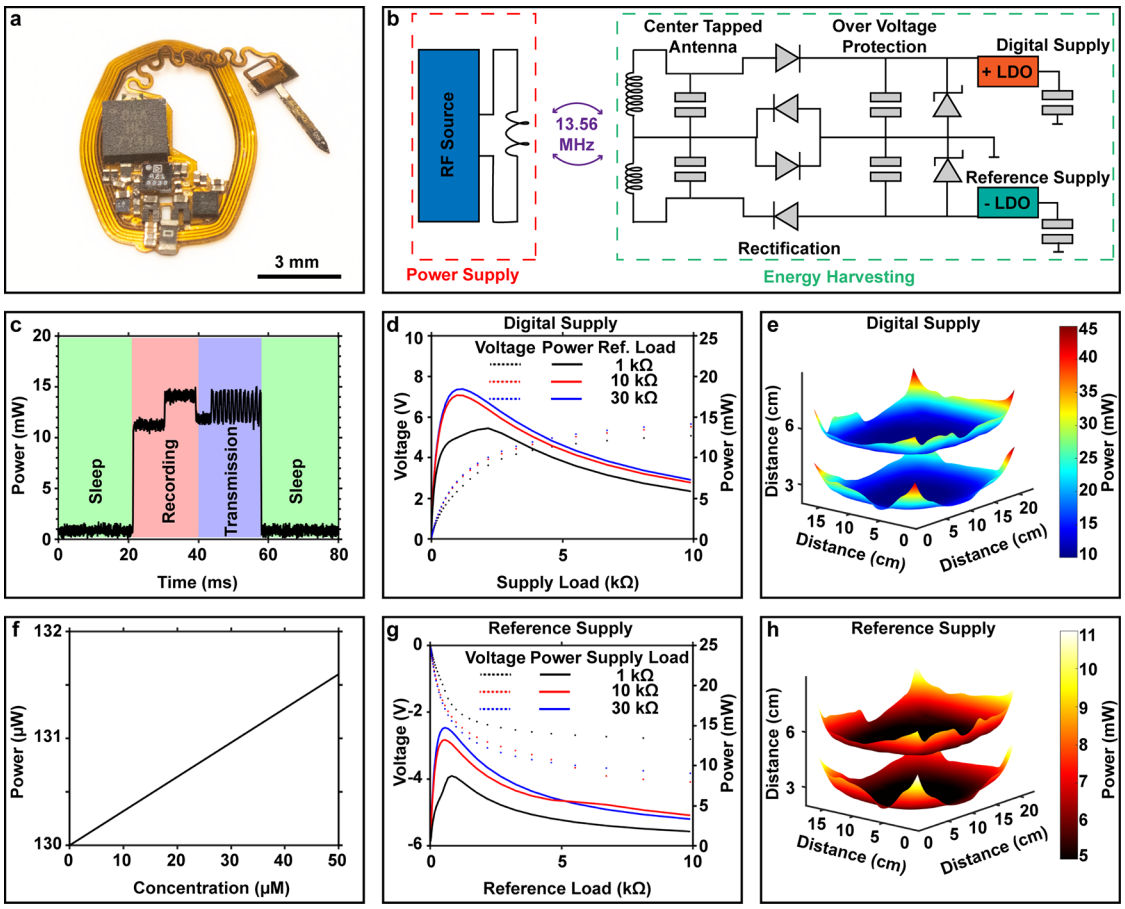

Figure 4. Power Harvesting: (a) Photographic image of device. (b) Electronic schematic for positive and negative voltage harvesting and stabilization. (c) Time resolved current consumption of the device during deep sleep (green), recording (red), and data transmission (blue). (d) Positive power vs load curve in the center of a 20 cm × 17 cm and 5 W input with varying positive and fixed negative loads. (e) Spatially resolved positive power harvesting of implantable device with a two-turn primary coil in a 20 cm × 17 cm cage and 5 W input power; reference supply is loaded with 1 MΩ. (f) Power consumption of negative supply with varying concentration of dopamine. (g) Negative power vs load curve in the center of a 20 cm × 17 cm and 5 W input with varying negative and fixed positive loads. (h) Spatially resolved negative power harvesting of implantable device with a two-turn primary coil in a 20 cm × 17 cm cage and 5 W input power; digital supply is loaded with 1 kΩ.

standard deviation of 6.48 mV (see Figure S8). This results in an estimated limit of detection of changes in dopamine concentration of 0.3 μM or more, sufficient to monitor DA dynamics across several experimental paradigms and procedures.[60−62]

Wireless and Battery-Free Dual Power Supply with Small Footprint. Critical to the device function and a substantial engineering challenge is the ability to provide a dual power supply in a footprint suitable for subdermal implantation in mice. To reduce the number of required components and displaced physiological volume during implantation, device functionality is achieved through implementation of a center tapped antenna structure that allows for both positive and negative voltage outputs for powering digital electronics and supplying reference voltages for the sensor, respectively. The device, shown in Figure 4a, features a 10-turn antenna structure with 100 μm traces and 50 μm spacings, with the positive and negative sides of the antenna containing 6 and 4 turns, respectively. This turn distribution is chosen to ensure maximum power point efficiency with operational voltages according to the anticipated load on each polarity of the power supply system, while optimizing the size of the device. Tuning of the antenna structure is carried out using 126 pF capacitors between the antenna tap and positive power output (see Figure 4b). Each side of the center tap utilizes a half wave rectifier to convert the incoming AC voltage into DC voltage with the respective polarity.

The digital circuitry consumes an average of 6.81 mW with peak consumption of 14 mW for 10 ms during stimulation and recording as shown in Figure 4c. A lower average power consumption is achieved by utilization of sleep events that selectively suspend microcontroller function. The antenna structure is optimized to harvest a peak positive power of 18.43 mW at 1.2 kΩ load on the positive coil and 30 kΩ load on the negative coil (see Figure 4d). Here, a 30 kΩ load is selected on the negative side to represent the highest load on the negative coil, given passive component requirements and average consumption of the RE. Because both negative and positive antennas are coupled electromagnetically, loading on either can affect efficiencies of the other. The antenna system is designed to only feature minimal effect on harvesting capability for operational ranges anticipated during recording. For example, for a loading of 10−30 kΩ of the negative supply, the digital supply is only minimally affected (Figure 4d). Three-dimensional mapping of power output was performed in

https://doi.org/10.1021/acsnano.2c09475
ACS Nano 2023, 17, 561−574

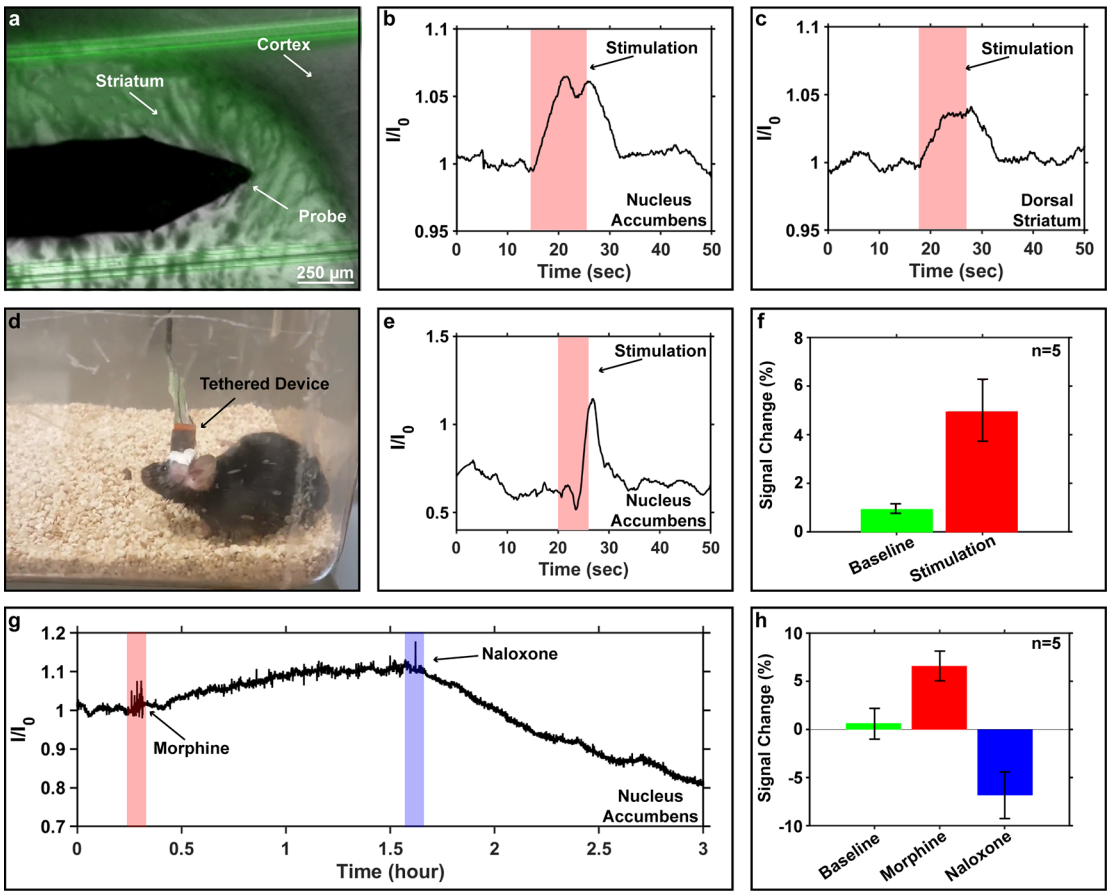

Figure 5. ***In Vitro*** **and** ***in Vivo*** **Tethered Optogenetic Stimulation and Recording: (a) Image illustrating the microneedle in contact with the striatum surrounded by ChR2-expressing dopamine axons in acute brain slices. (b) DA transients captured by the microneedle upon optical stimulation (red) of the nucleus accumbens slices.** ***Y*****-axis scale = 250 nM. (c) DA transients captured by the sensor upon optical stimulation (red) of the dorsal striatum slices.** ***Y*****-axis scale = 250 nM. (d) Image of mouse with tethered recording system. (e) Data recorded from continuous collection of tethered moving subjects with an optogenetically enabled probe. (f) Signal change during baseline recordings and stimulation in a cohort of five animals. (g) Variation in DA concentration in the nucleus accumbens region in a tethered subject after administering morphine (10 mg/kg s.c.) and naloxone (3 mg/kg s.c.). (h) Signal change in response to psychostimulant injections in a cohort of five animals.**

a large cage (20 cm × 17 cm) at heights of 3 and 6 cm to simulate physiological positions of the animal during normal motion and rearing, respectively.[63] With a 5 W RF input power (up to 10 W of RF power is within FCC approved power in commercially sold devices),[4,64] the device can harvest 15.2 mW of power at the center of the cage, demonstrating efficient operation across operational space (see Figure 4e). The power consumption of the reference electrode from the DA sensor demonstrates linear dependency on the measured DA concentration.

Figure 4f shows the power consumption of the system across physiological ranges of DA concentration in the brain ranging from 130 to 132 μW. A peak power output of 14.7 and 7.3 mW is achieved with loads on the positive antenna of 30 and 1 kΩ, respectively. These loads are chosen to represent load on the system during deep sleep and stimulation, respectively. Figure 4g shows the load curve for the negative coil with varying positive loads. Here, the antenna structure is optimized to harvest 14.8 and 7.6 mW at 700 Ω load with a positive load of 30 and 1 kΩ, respectively. Here, it is important to note that the load on the negative coil operates around 30 kΩ yet can supply adequate power due to the low powering and voltage requirements of the biasing circuit. Figure 4h shows a three-dimensional mapping of power output performed in a large cage (20 cm × 17 cm) at heights of 3 and 6 cm. Negative voltage output from the center tapped antenna supplies more than sufficient power for this application, with 0.9 mW output at the center of large cage (5 W input power). With the implementation of center tapped antenna structure in this small form factor, stable voltage supplies for both digital electronics and reference voltages can be achieved in large arenas (<55 cm^2) hosting freely moving subjects. For applications requiring larger arena footprints, RF power can be increased to meet demands.[65]

In Vitro and in Vivo Tethered Optogenetic Stimulation and Real-Time Dopamine Recording. To test the sensor function and ability to detect synaptic release of dopamine in the brain, we used transgenic mice to express the light sensitive protein, channelrhodopsin-2 (ChR2-YFP) in all dopamine neurons (DAT-Cre x ai32, see the Methods section). Acute slices of the brain show ChR2-YFP traffics efficiently along dopamine axons in the striatum, where the probe is placed in either the dorsal striatum or nucleus accumbens (Figure 5a). After baseline recording, optogenetic stimulation of ChR2 with blue light (470 nm, 20 Hz, 1 ms pulse-width), produces a rapid and reversible increase in DA

https://doi.org/10.1021/acsnano.2c09475
ACS Nano 2023, 17, 561−574

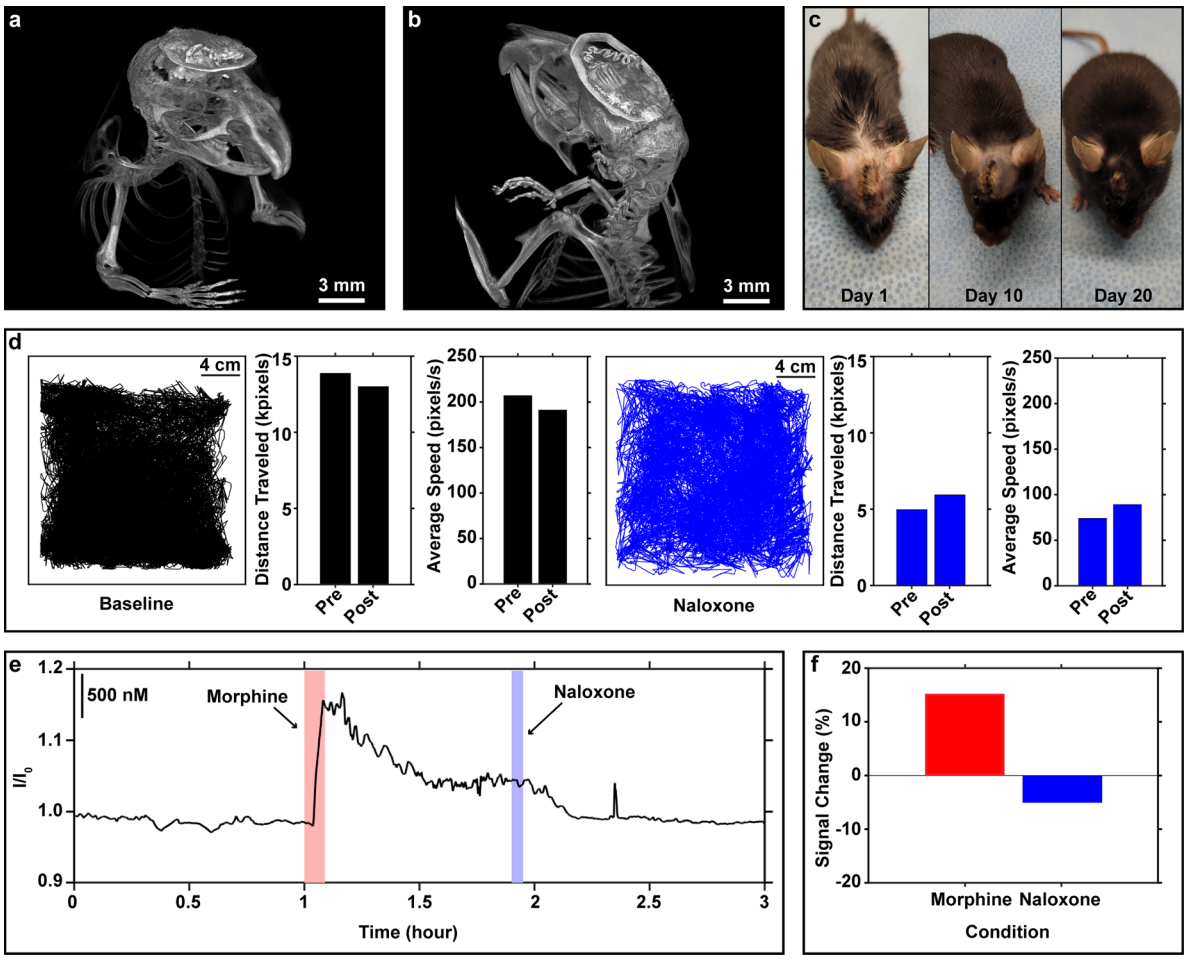

Figure 6. Wireless Battery-Free Recording in Freely Moving Subjects: (a) Anterior micro-CT image of the subdermally implanted device. (b) Posterior view micro-CT of subject showing conformal application of the device to skull. (c) Photographic images of scar healing of subjects 1, 10, and 20 days after implantation surgery. (d) Behavioral study results comparing distance traveled during baseline and naloxone injection pre- and postimplantation. (e) Wireless, *in vivo* recording showing dopamine response in the nucleus accumbens during morphine injection (10 mg/kg s.c.) and subsequent naloxone injection (3 mg/kg s.c.) (f) Resulting signal change after psychostimulant and narcotic injections.

transients in both the nucleus accumbens (Figure 5b) and dorsal striatum (Figure 5c). Data from additional brain slices appear in Figure S9. These studies reveal that the nanocomposite sensor can capture fast DA transients with excellent reversibility.

In vivo performance of the sensor is evaluated with a tethered system set up in DAT-Cre x Ai32 mice (Figure 5d). The sensor is implanted into the nucleus accumbens and tethered to an external potentiostat for recording. After baseline measurements were recorded, we administered brief 5 s optogenetic stimulation of ChR2 with blue LED on the sensor (470 nm, 20 Hz, 1 ms pulse-width) to recapitulate the catecholamine transients observed in our acute slice recordings (Figure 5e). Studies are repeated in a cohort of five subjects, with results compiled in Figure 5f. Sensor performance is repeatable with an average signal change of 1.05 I/I_0 resulting in a total signal change of 5% in dopamine levels with a standard deviation of ±1.9% in signal during stimulation and 1.2% signal change with a standard deviation of ±0.9% in baseline. Social interaction studies are also conducted, which show a DA response to subject interaction (see Figure S10).

Changes in dopamine concentration also occur with the administration of opiate analgesics and opiate antagonists.[66−70] After baseline measurements are recorded, the subject is administered morphine (10 mg/kg s.c.), resulting in a robust increase in DA transients (Figure 5g). With subsequent administration of naloxone (3 mg/kg s.c.), an opiate antagonist reverses the measured DA concentration below baseline levels. Studies are repeated in a cohort of five subjects (see Figure 5h), which result in an average 6.4% increase in signal from baseline with administration of morphine (SD = 1.7%). With the administration of naloxone, a −6.7% decrease in signal from baseline is recorded, which correlates to a 13.1% decrease in signal from morphine levels (SD = 2.5%).

Dopamine Monitoring in Freely Moving Subjects. Performance of the tethered system performed with state-of-the-art potentiostats is validated against fully implantable systems in freely behaving subjects. *In vivo* recordings are conducted using C57BL/6j mice. Devices are implanted subdermally with the body of the device affixed to the skull and sensor inserted into the nucleus accumbens (details in the Methods section). Figure 6a shows a μCT image of a subject after implantation with the device. Figure 6b shows the device from posterior view indicating conformal lamination to the skull that enables suturing of the skin over the implantation site without any externalization of hardware substantially reducing

https://doi.org/10.1021/acsnano.2c09475
ACS Nano 2023, 17, 561−574

infection risk. Postimplantation monitoring shows complete recovery after 20 days, (see Figure 6c). This subdermal form factor facilitates several experimental paradigms that include cohabitation of subjects, enabling studies of social interaction and other paradigms that require extensive subject movement and preclude externalized hardware because of grooming among littermates that results in hardware damage.

To illustrate the response of the wireless and battery-free device, an experiment designed to test changes in DA levels in the nucleus accumbens in response to opiate analgesics (morphine) and opiate antagonists (naloxone) is performed.[71] Recordings are collected 1 h after the animal is removed from anesthesia. The subjects are observed for approximately 1 h prior to injection of morphine (10 mg/kg s.c.) with subsequent injection of naloxone (3 mg/kg s.c.).

Behavioral analysis derived from these experiments is shown in Figure 6d. Here, subject motion is tracked with a camera and features are extracted using deep neural networks as described in the Methods section. Behavior of the same subject is captured preimplantation and 25 days postimplantation after surgical recovery. Subject motion as shown in the trajectory maps indicate similar patterns before and after device implantation, with total distance traveled exhibiting little variation. This demonstrates a key aspect of the device architecture that poses minimal impact on subject behavior and eliminates baseline studies to normalize for effects of either tethers or externalized battery powered equipment. The high fidelity of behavioral recordings can also be used to measure effect of drugs as shown in Figure 6d. Implantation of the device results in a negligible effect on subject behavior in both distance traveled and speed. The impact of opiate antagonists resulting in a significant reduction in locomotion after administration of naloxone can also clearly be observed.[72,73] Important to note is that in both the control and opiate antagonist cases the device does not impact the behavior of the subject.

Results from dopamine recordings *in vivo* are shown in Figure 6e. After baseline measurements, the subject is injected with morphine, which results in a 15% increase in signal recording from baseline. This initial increase then reaches a steady state 30 min post injection, resulting in a steady state increase of 6%. It is important to note that response to dopamine injection is animal dependent, resulting in varying transient dynamics and response times.[74,75] After 45 min, the subject is injected with naloxone, resulting in a reduction of dopamine concentration back to baseline levels (see Figure 6f). The results compare with tethered experiments using a benchtop potentiostat with an estimated LOD of 0.317 μM, further highlighting the performance of the highly miniaturized solution that enables full subdermal implantation.

CONCLUSION

In summary we introduce a wireless and battery-free device designed for subdermal implantation, which is capable of simultaneous optogenetic stimulation and electrochemical recordings of catecholamine dynamics. The devices are enabled by advances in materials and electronics to deliver system functionality that would otherwise require large, battery-powered, or tethered device schemes substantially impacting the ability to perform experiments in naturalistic environments and chronic time scales. The complete device only occupies a volume of 12 × 8.5 × 3.2 mm^3 and features a weight of 49 mg, which reduces the device footprint compared to battery and externalized power supplies previously reported systems by 79% and 98%, respectively.[24,36] The introduction of a power harvesting scheme using a center tapped antenna allows for harvesting of positive and negative voltage potentials needed to power digital electronics and analog biasing circuits, which in combination with the injectable electrochemical sensor based on a SWCNT-CF composite material features one of the highest sensitivities for a sensor of similar classification[76] and enables a completely battery free continuous operation (see Table S1). Capabilities of the system are demonstrated in freely behaving subjects providing both optogenetic stimulation capabilities and real-time catecholamine level readouts. Features demonstrated here enable advanced dissection of the central nervous system with cell and catecholamine specificity without affecting the behavior of the subjects providing advanced tools to uncover fundamental mechanisms of neurological disease. Wireless and battery-free operation of the device enables chronic observation of catecholamine dynamics in real time, which yet require developments of protocols to study chronic stability *in vivo* effectively.

METHODS

Probe Fabrication. Probe fabrication began with first pattering a flexible copper/poylimide/Cu substrate (DuPont Pyralux AP8535R) using a UV (355 nm) laser ablation system (LPKF; Protolaser U4) to form the contact pads for the blue μ-LED, WE, and RE and conducting traces for the μ-LED. Next, the μ-LED was soldered onto the probe followed by parylene coating (thickness 14 μm) the entire probe except the contact pads. The subsequent step involved electron beam deposition of titanium (thickness: 20 nm) and gold (thickness: 150 nm) using a polyimide-based shadow mask to form the current collector for the WE. Next, a tungsten film (thickness: 50 μm) was attached to the back end of the shaft of the probe using a fast-curing epoxy to impart rigidity to the probe for facilitating easy insertion into the target tissue. Thereafter a second overcoat of parylene (thickness: 14 μm) encapsulated the full device. Reactive ion etching of the parylene through a polyimide-PDMS shadow mask selectively exposed the contact pads and the tip of the Au layer (~400 × 400 μm^2), which served as the conductive electrode for the bonding the SWCNT-CF composite electrode. This step was followed by fabrication of the RE, which included painting a thin layer of Ag/AgCl ink (Ercon Inc.) on the parlyene coated tungsten piece attached to the back of the probe and baking at 80 °C for 20 min. The SWCNT-CF composite electrode (fabrication details below) was then bonded to the exposed gold tip using commercial carbon ink (Ercon Ink) as a glue followed by baking at 80 °C for 20 min. Finally, the entire probe was dip coated in Nafion solution (2.5 wt % prepared in isopropyl alcohol) for 10 s and baked for 10 min at 80 °C. Three such layers were formed.

The fabrication of the SWCNT-CF composite electrode involved the following steps. First, commercial CF film (FuelCell Store; Toray paper 030, 5 wt % wet proofed) was first treated with a corona treater (2 min each side) to improve its hydrophilicity. Next, a 100 mg/mL suspension of milled CF (ZOLTEK Corp) in 3 wt % solution of chitosan (high molecular weight, Sigma-Aldrich) prepared in 1 M acetic acid was spin coated (speed, 200 rpm; time, 30 s) on one side of the CF film followed by baking at 100 °C for 10 min. This step was repeated on the other side of the CF film. Thereafter, the sample was transferred into a rapid thermal processing machine in which it was first heated at 600 °C for 15 min in air followed by heating at 1000 °C for 5 min in a nitrogen environment. The next step involved coating the film with three layers of carboxylic-functionalized SWCNTs (Cheaptubes Inc.) suspension prepared in 1 wt % nafion solution in deionized water. After each dip coating, the film was baked at 90 °C for 10 min. The SWCNT suspension was prepared by probe

https://doi.org/10.1021/acsnano.2c09475
ACS Nano 2023, 17, 561−574

sonication. Finally, the films were diced into 0.4 x 0.4 mm^2 electrodes using a picosecond laser (LPKF; Protolaser U4).

Device Fabrication. Devices were designed on a panel structure and sent for external manufacturing. The flexible PCB panels were fabricated using one layer of polyimide (30 μm) between two layers of copper (35 μm). Devices structures were depaneled using a UV (355 nm) laser ablation system (LPKF; Protolaser U4). Depaneled devices were then cleaned *via* sonication (Vevor; 2L Ultrasonic Cleaner) with isopropanol (IPA). Surface mounted devices were manually placed and reflowed with low temperature solder paste (Chip Quik; TS391LT). Probes were attached to the device using silver epoxy (MG Chemicals; 8331D) and then cured at 60 °C for 1 h. After assembly, components and probe attachments were fixed into place with UV-curable glue (Damn Good; 20910DGFL), followed by curing with a UV lamp (24 W) for 5 min and degassing in an oven for 5 min at 100 °C.

Device Tuning and Design. Commercially available components were placed by hand and reflowed using low-temperature solder paste (Chip Quik; TS391LT). A rectifier with a center tap was constructed using Schottky diodes (40 V, 30 mA, MCC RB751S-40DP) and assorted 0201 footprint capacitors (TDX) for tuning and rectification, while a 0603 0Ω resistor (Vishay Dale) was used to provide the center tap. The number of coils on each side of the device was modulated for negative and positive power requirements. Tuning capacitors were placed on the positive coil and were chosen to produce the lowest voltage standing wave ratio at 13.56 MHz using a reflection bridge (Siglent; SSA 3032X). Zener diodes (5.6 V, 100 mW, Comchip CZRZ5 V6B-HF) were used for overvoltage protection on both sides of the center tapped antenna. Low-dropout regulators with fixed internal outputs (3.3 V; ON Semiconductor; NCP163AFCT330T2G. −1.1 V; Nisshinbo; RP117 K111D-TR) managed system and reference electrode voltages, respectively. A dual operational amplifier (Analog Devices; ADA4505-2) was used in a transimpedance and noninverting configuration to detect and amplify changes in current from the probe, which was then digitized by a microcontroller (Atmel; ATTiny84A). The digital signal was modulated at 57 kHz and transmitted using a current limited 0402 IR LED (Everlight Electronics Co Ltd.; IR16−213C/L510/TR8).

Encapsulation. Prior to encapsulation, tips of the probes were covered with polyimide sheets and sealed with parafilm to create an airtight seal and protect the probe surface from the encapsulation procedure. The devices were suspended on a thin wire and encapsulated using a Paralyene P6 vapor deposition system (Diener electronic GmbH) to achieve a total encapsulation thickness of ∼18 μm. The encapsulation thickness was estimated from measurements using a profilometer (KLA; Tencor P15). After encapsulation, devices were dip coated with PDMS (SYLGARD; 184 Silicone Elastomer kit) and cured at 80 °C for 24 h. Afterward, probe coverings were removed by hand and device functionality was tested on the benchtop.

Power Harvesting Characterization. Voltage and power harvesting of the antenna was conducted on a device populated with tuning capacitors, Schottky diodes, and a smoothing capacitor. The devices were placed in the center of a 20 cm × 17 cm arena and powered with a dual loop antenna set to 5 W of RF power. To generate load curves, variable shunt resistors were used to modulate load on both the positive and negative outputs while the resulting voltage was measured using two oscilloscopes (Siglent; SDS 1202X-E). In addition, positive and negative voltage measurements were taken in the center of the box while tilting the board from 0 to 90° about its horizonal (pitch) and vertical (roll) axis. For arena characterization, shunt resistors of 1 kΩ load and a 1 MΩ load were used to simulate the load seen by the positive and negative voltages, respectively. The device was fixed to 3D printed boxes with varying heights (3 and 6 cm), which were moved about the arena to collect spatial power harvesting data. The device's current consumption was recorded using a current meter (LowPowerLab; CurrentRanger) and acquired using an oscilloscope (Siglent; SDS 1202X-E).

Motion Artifact Testing. To test the effect of motion artifacts and serpentine interconnect on sensor output, a 10 MΩ resistor was attached between the working and reference electrodes. The device was then mounted in a custom stretching stage, which allowed for displacement of the serpentine structure with simultaneous wireless power transfer and IR data recording. The serpentine was displaced by 60% for 1000 cycles with simultaneous data recording (see Figure S4).

Wireless Benchtop Experiments. Phosphate buffered saline (PBS) (pH 7, 0.1 M) was prepared by dissolving premade PBS tablets (Life Technologies; 003002) into 1 L of deionized and stirring for 10 min. Devices were placed in a 15 cm × 15 cm arena and suspended using a 3D printed support. A small beaker was placed into the arena and filled with 4 mL of PBS. The probe was inserted into the solution using a stereotactic clip while the device was held into place (see Figure S8), and a baseline recording was taken for 10 min. A stock solution of 10 mM dopamine was created by dissolving 15.3 mg of dopamine hydrochloride into 10 mL of PBS. The dopamine solution was immediately diluted to 1 mM by adding 100 μL of 10 mM solution to 900 μL of PBS. Once the baseline reading was established, 20 μL of PBS was removed from the working solution and replaced with 20 μL of 1 mM dopamine solution to increase the working solutions concentration by 5 μM. This procedure was repeated until the desired final solution concentration was obtained.

Subjects and Surgical Procedures. For *ex vivo* recordings, DAT-Cre mice (PMID 15763133) were crossed to the homozygous Ai32 line (PMID 22446880) for Cre-dependent expression of ChR2-eYFP in dopamine neurons. C57BL/6j mice 7−10 weeks of age bred in-house for all *in vivo* experiments. Mice were housed in the animal facilities of the Washington University School of Medicine on a 12 h light/dark cycle, with access *ad libitum* to food and water. Device implantation: once male mice were fully anesthetized using 1.5%−2% isoflurane, their scalps were shaved and sterilized. Mice were then positioned on a stereotactic frame (David Kopf Instruments, Tujunga, CA) equipped with a heating pad to maintain body temperature throughout the procedure. Preoperative care consisted of an application of sterile eye ointment, subcutaneous injection of 1 mL of sterile saline, and surgery site sterilization with iodine. During the surgery, anesthesia was maintained using 1%−2% isoflurane. A midline incision was made to expose the skull. A variable-speed surgical drill was used to create a hole above the target implant region and through the skull (until the dura was reached). Using the attachment flag, the probe was stereotactically lowered into the nucleus accumbens region (1.2 mm from bregma, 1.0 mm from midline, and 4.6 mm ventral to skull) at a rate of ∼100 μm s^{-1} until appropriately positioned. The flag and probe were then affixed to the skull using cyanoacrylate or dental cement to prevent device dislocation. To fully secure the implant, the body of the probe was fixed to the surface of the skull using dental cement. The device was then enclosed and sutured underneath the scalp. Postoperative care also included application of topical triple antibiotic ointment and 2% lidocaine. All mice were monitored on a heating pad until fully recovering from anesthetization. Mice were allowed to fully recover from anesthetization prior to behavioral experiments. All experimental procedures were conducted in accordance with the National Institutes of Health standards and were approved by the Institutional Animal Care and Use Committees at Washington University.

In Vitro Recordings. Acute brain slices of the striatum were prepared as described.[77] After transcranial perfusion with cold NMDG-aCSF, 300 μm thick coronal sections were cut with a Compresstome, transferred into NMDG-aCSF at 32 °C for 10 min, and then held at room temperature in standard aCSF until recording. Slices were transferred to an upright microscope and visualized using IR-DIC microscopy. Probes were mounted onto manipulators and slowly lowered onto the striatum. Widefield photostimulation was delivered through a 4× objective using a blue LED (Thorlabs; M470L2) coupled to the back fluorescence port of the microscope.

Tethered Recordings. Animals were allowed to recover from isoflourane anesthesia and then tethered to an external potentiostat. For social interaction experiments, a mouse was placed in the cage

https://doi.org/10.1021/acsnano.2c09475
ACS Nano 2023, 17, 561−574

with the tethered animal and the timing of interactions were compared with dopamine values. For the evaluation of morphine-induced catecholamine release, morphine was subcutaneously administered at 10 mg/kg. To antagonize the effects of morphine, naloxone (3 mg/kg s.c.) was then administered. Before the recordings were performed, mice were habituated in their home cages for 1 h with tether connected to the implanted sensor. For recording catecholamine transients from the sensor, mice were then placed in the open field arena (55 × 55 cm^2) during trials and allowed to freely explore after the experimenter exited the room (behaviors were video recorded).[78] For social behaviors, after stable baseline recordings were obtained, we introduced an unfamiliar female mouse and obtained recordings from sensor during their interactions. Behaviors were video recorded and analyzed using DeepLabCut Version 2.2.b6.[79]

Wireless Dopamine Recordings in Freely Moving Animals. Once animals had recovered from anesthesia, they were placed into a recording chamber (12 cm × 12 cm × 12 cm) equipped with Neurolux antenna systems (Evanston, IL) to verify function. One hour after the animals were removed from anesthesia, the animals were placed back into the recording chamber for experiments. Once the device connection to the receiver was confirmed, baseline measurements were recorded for 1 h. Animals were next injected with morphine (10 mg/kg s.c.) and recorded for 1 h. Finally, animals were injected with naloxone (3 mg/kg s.c.) and recorded for 1 h. The recording was then stopped, and the animal placed back in its home cage.

Behavioral Analysis. Video were recorded using a camera (Google; Pixel 6) mounted above the arena. Tracking of the head's position was performed using DeepLabCut Version 2.2.b6.[79] To monitor the animal's movement, the head, both ears, and the tail were selected for feature tracking. One hour videos were collected for each condition, namely, baseline, post morphine injection, and post naloxone injection. Model training was performed using a high-performance computer (University of Arizona; HPC) with 100,000 iterations. Results from the computed tracking were exported in a comma separated value document containing pixel position and confidence values for each tracked feature. Positional data that obtained a confidence value greater than 99% were used for behavioral analysis. This data was fed into MATLAB where the total distance traveled was calculated and heat maps of animal movement over time were plotted.

μCT Imaging. μCT imaging was performed on post-mortem subjects preserved with flash freezing. Images were acquired using a Siemens Inveon μ-CT scanner. "Medium-high" magnification, an effective pixel size of 23.85, 2 × 2 binning, with 720 projections made in a full 360° scan, along with an exposure time of 300 ms were used.

ASSOCIATED CONTENT

Supporting Information

The Supporting Information is available free of charge at https://pubs.acs.org/doi/10.1021/acsnano.2c09475.

Figures of wireless and battery-free device design, annotated device design with a list of components used, plot of device data rate across the experimental arena, images and data sets showing serpentine deformation effect on sensor, additional SEM micrographs and characterization, Nafion coating characterization, sensor performance characterization, benchtop, wireless sensor performance data, additional wired *in vivo* data, and animal behavioral experiments and table of sensor sensitivities found in the literature (PDF)

AUTHOR INFORMATION

Corresponding Authors

Vijay K. Samineni − *Department of Anesthesiology and Washington University Pain Center, Washington University School of Medicine, St. Louis, Missouri 63110, United States*; Email: vksamineni@wustl.edu

Amay J. Bandodkar − *Department of Electrical and Computer Engineering and Center for Advanced Self-Powered Systems of Integrated Sensors and Technologies (ASSIST), North Carolina State University, Raleigh, North Carolina 27606, United States*; orcid.org/0000-0002-1792-1506; Email: ajbandod@ncsu.edu

Philipp Gutruf − *Department of Biomedical Engineering, Department of Electrical and Computer Engineering, Bio5 Institute, and Neuroscience GIDP, University of Arizona, Tucson, Arizona 85721, United States*; Email: pgutruf@arizona.edu

Authors

Tucker Stuart − *Department of Biomedical Engineering, University of Arizona, Tucson, Arizona 85721, United States*; orcid.org/0000-0002-4643-6868

William J. Jeang − *Department of Materials Science and Engineering, Northwestern University, Evanston, Illinois 60201, United States*; orcid.org/0000-0002-5401-8535

Richard A. Slivicki − *Department of Anesthesiology and Washington University Pain Center, Washington University School of Medicine, St. Louis, Missouri 63110, United States*

Bobbie J. Brown − *Department of Anesthesiology and Washington University Pain Center, Washington University School of Medicine, St. Louis, Missouri 63110, United States*

Alex Burton − *Department of Biomedical Engineering, University of Arizona, Tucson, Arizona 85721, United States*; orcid.org/0000-0001-7182-0696

Victoria E. Brings − *Department of Anesthesiology and Washington University Pain Center, Washington University School of Medicine, St. Louis, Missouri 63110, United States*

Lilian C. Alarcón-Segovia − *Querrey Simpson Institute for Bioelectronics, Northwestern University, Evanston, Illinois 60201, United States*

Prophecy Agyare − *Department of Neuroscience, Northwestern University, Evanston, Illinois 60201, United States*

Savanna Ruiz − *Department of Materials Science and Engineering, Northwestern University, Evanston, Illinois 60201, United States*

Amanda Tyree − *Department of Biomedical Engineering, University of Arizona, Tucson, Arizona 85721, United States*

Lindsay Pruitt − *Department of Biomedical Engineering, University of Arizona, Tucson, Arizona 85721, United States*

Surabhi Madhvapathy − *Department of Materials Science and Engineering, Northwestern University, Evanston, Illinois 60201, United States*

Martin Niemiec − *Department of Biomedical Engineering, University of Arizona, Tucson, Arizona 85721, United States*

James Zhuang − *Department of Biomedical Engineering, University of Arizona, Tucson, Arizona 85721, United States*

Siddharth Krishnan − *Querrey Simpson Institute for Bioelectronics, Northwestern University, Evanston, Illinois 60201, United States*

Bryan A. Copits − *Department of Anesthesiology and Washington University Pain Center, Washington University School of Medicine, St. Louis, Missouri 63110, United States*

John A. Rogers − *Department of Materials Science and Engineering, Querrey Simpson Institute for Bioelectronics, Department of Mechanical Engineering, Department of Biomedical Engineering, and Department of Neurological*

Surgery, Feinberg School of Medicine, Northwestern University, Evanston, Illinois 60201, United States; Department of Neurological Surgery and Center for Bio-Integrated Electronics, Northwestern University, Evanston, Illinois 60208, United States; orcid.org/0000-0002-2980-3961

Robert W. Gereau, IV − *Department of Anesthesiology and Washington University Pain Center, Washington University School of Medicine, St. Louis, Missouri 63110, United States; Department of Neuroscience and Department of Biomedical Engineering, Washington University, St. Louis, Missouri 63110, United States*

Complete contact information is available at: https://pubs.acs.org/10.1021/acsnano.2c09475

Author Contributions

A.J.B., V.K.S., and P.G. conceived the experiments. W.J.J., L.C.A.-S., P.A., S.R., S.M., S.K., and A.J.B. designed, fabricated, and characterized the probe. T.S., M.N., J.Z., and A.B. designed the analog front end. T.S., M.N., J.Z., L.P., A.T., and A.B. characterized and tested the analog front end. T.S., A.B., M.N. and J.Z. designed the device. T.S., A.T., A.B., M.N., and L.P. fabricated the device. T.S., A.T., and L.P. characterized device performance. T.S., M.N., and A.B. designed and performed benchtop device experiments. B.A.C. performed acute slice recordings. V.K.S., R.S., B.J.B., T.S., and V.E.B. performed behavioral analysis. T.S., J.A.R., R.W.G., A.J.B., V.K.S., and P.G. wrote and reviewed the manuscript with comments from all the authors.

Funding

P.G. acknowledges support from Arizona Technology and Research Initiative Fund and startup funds from Department of Biomedical Engineering at the University of Arizona. R.A.S. acknowledges support from F32DA051160. B.J.B. acknowledges support from the Howard Hughes Medical Institute Gilliam Fellowship. V.K.S. acknowledges support from NIDDK K01 DK115634 and R01DK128475. R.W.G. acknowledges support from R01DK116178 and R01NS106953.

Notes

The authors declare no competing financial interest.

ACKNOWLEDGMENTS

The authors thank Brenda Baggett for assistance with micro-CT collection.

REFERENCES

(1) Vázquez-Guardado, A.; Yang, Y.; Bandodkar, A. J.; Rogers, J. A. Recent Advances in Neurotechnologies with Broad Potential for Neuroscience Research. *Nat. Neurosci.* **2020**, *23*, 1522−1536.

(2) Chen, Y.; Rommelfanger, N. J.; Mahdi, A. I.; Wu, X.; Keene, S. T.; Obaid, A.; Salleo, A.; Wang, H.; Hong, G. How Is Flexible Electronics Advancing Neuroscience Research? *Biomaterials* **2021**, *268*, 120559.

(3) Gutruf, P.; Krishnamurthi, V.; Vázquez-Guardado, A.; Xie, Z.; Banks, A.; Su, C.-J.; Xu, Y.; Haney, C. R.; Waters, E. A.; Kandela, I.; Krishnan, S. R.; Ray, T.; Leshock, J. P.; Huang, Y.; Chanda, D.; Rogers, J. A. Fully Implantable Optoelectronic Systems for Battery-Free, Multimodal Operation in Neuroscience Research. *Nat. Electron* **2018**, *1* (12), 652−660.

(4) Gutruf, P.; Rogers, J. A. Implantable, Wireless Device Platforms for Neuroscience Research. *Curr. Opin Neurobiol* **2018**, *50*, 42−49.

(5) Da, Y.; Luo, S.; Tian, Y. Real-Time Monitoring of Neurotransmitters in the Brain of Living Animals. *ACS Appl. Mater. Interfaces*, in press, **2022**.

(6) Moraldo, C.; Vuille-dit-Bille, E.; Shkodra, B.; Kloter, T.; Nakatsuka, N. Aptamer-Modified Biosensors to Visualize Neurotransmitter Flux. *J. Neurosci Methods* **2022**, *365*, 109386.

(7) Wise, R.; Dopamine, A. Learning and Motivation. *Nat. Rev. Neurosci* **2004**, *5* (6), 483−494.

(8) Chakravarthy, S.; Balasubramani, P. P.; Mandali, A.; Jahanshahi, M.; Moustafa, A. A. The Many Facets of Dopamine: Toward an Integrative Theory of the Role of Dopamine in Managing the Body's Energy Resources. *Physiol Behav* **2018**, *195*, 128−141.

(9) Ferreri, L.; Mas-Herrero, E.; Zatorre, R. J.; Ripollés, P.; Gomez-Andres, A.; Alicart, H.; Olivé, G.; Marco-Pallarés, J.; Antonijoan, R. M.; Valle, M.; et al. Dopamine Modulates the Reward Experiences Elicited by Music. *Proc. Natl. Acad. Sci. U. S. A.* **2019**, *116* (9), 3793−3798.

(10) Pan, X.; Kaminga, A. C.; Wen, S. W.; Wu, X.; Acheampong, K.; Liu, A. Dopamine and Dopamine Receptors in Alzheimer's Disease: A Systematic Review and Network Meta-Analysis. *Front. Aging Neurosci.* **2019**, *11*, 175.

(11) Martorana, A.; Koch, G. Is Dopamine Involved in Alzheimer's Disease? *Front. Aging Neurosci.* **2014**, *6*, 252.

(12) Mitchell, R. A.; Herrmann, N.; Lanctôt, K. L. The Role of Dopamine in Symptoms and Treatment of Apathy in Alzheimer's Disease. *CNS Neurosci Ther* **2011**, *17* (5), 411−427.

(13) Masato, A.; Plotegher, N.; Boassa, D.; Bubacco, L. Impaired Dopamine Metabolism in Parkinson's Disease Pathogenesis. *Mol. Neurodegeneration* **2019**, *14* (1), 1−21.

(14) Goldstein, D. S.; Holmes, C.; Lopez, G. J.; Wu, T.; Sharabi, Y. Cerebrospinal Fluid Biomarkers of Central Dopamine Deficiency Predict Parkinson's Disease. *Parkinsonism Relat Disord* **2018**, *50*, 108−112.

(15) Meder, D.; Herz, D. M.; Rowe, J. B.; Lehéricy, S.; Siebner, H. R. The Role of Dopamine in the Brain-Lessons Learned from Parkinson's Disease. *Neuroimage* **2019**, *190*, 79−93.

(16) Cummings, J. L. Depression and Parkinson's Disease: A Review. *Am. J. Psychiatry* **1992**, *149* (4), 443−454.

(17) Schwerdt, H. N.; Zhang, E.; Kim, M. J.; Yoshida, T.; Stanwicks, L.; Amemori, S.; Dagdeviren, H. E.; Langer, R.; Cima, M. J.; Graybiel, A. M. Cellular-Scale Probes Enable Stable Chronic Subsecond Monitoring of Dopamine Neurochemicals in a Rodent Model. *Commun. Biol.* **2018**, *1* (1), 1−11.

(18) Li, J.; Liu, Y.; Yuan, L.; Zhang, B.; Bishop, E. S.; Wang, K.; Tang, J.; Zheng, Y.-Q.; Xu, W.; Niu, S.; Beker, L.; Li, T. L.; Chen, G.; Diyaolu, M.; Thomas, A.-L.; Mottini, V.; Tok, J. B.-H.; Dunn, J. C. Y.; Cui, B.; Paşca, S. P.; Cui, Y.; Habtezion, A.; Chen, X.; Bao, Z. A Tissue-like Neurotransmitter Sensor for the Brain and Gut. *Nature* **2022**, *606* (7912), 94−101.

(19) Shao, Z.; Chang, Y.; Venton, B. J. Carbon Microelectrodes with Customized Shapes for Neurotransmitter Detection: A Review. *Anal. Chim. Acta* **2022**, *1223*, 340165.

(20) Niyonambaza, S. D.; Kumar, P.; Xing, P.; Mathault, J.; de Koninck, P.; Boisselier, E.; Boukadoum, M.; Miled, A. A Review of Neurotransmitters Sensing Methods for Neuro-Engineering Research. *Applied Sciences* **2019**, *9* (21), 4719.

(21) Zhao, C.; Cheung, K. M.; Huang, I.-W.; Yang, H.; Nakatsuka, N.; Liu, W.; Cao, Y.; Man, T.; Weiss, P. S.; Monbouquette, H. G.; Andrews, A. M. Implantable Aptamer−Field-Effect Transistor Neuroprobes for in Vivo Neurotransmitter Monitoring. *Sci. Adv.* **2021**, *7* (48), eabj7422.

(22) Gao, Z.; Wu, G.; Song, Y.; Li, H.; Zhang, Y.; Schneider, M. J.; Qiang, Y.; Kaszas, J.; Weng, Z.; Sun, H.; Huey, B. D.; Lai, R. Y.; Zhang, Y. Multiplexed Monitoring of Neurochemicals via Electrografting-Enabled Site-Selective Functionalization of Aptamers on Field-Effect Transistors. *Anal. Chem.* **2022**, *94* (24), 8605−8617.

(23) Lu, L.; Gutruf, P.; Xia, L.; Bhatti, D. L.; Wang, X.; Vazquez-Guardado, A.; Ning, X.; Shen, X.; Sang, T.; Ma, R.; Pakeltis, G.; Sobczak, G.; Zhang, H.; Seo, D.-O.; Xue, M.; Yin, L.; Chanda, D.;

Sheng, X.; Bruchas, M. R.; Rogers, J. A. Wireless Optoelectronic Photometers for Monitoring Neuronal Dynamics in the Deep Brain. *Proc. Natl. Acad. Sci. U. S. A.* **2018**, *115* (7), E1374−E1383.
(24) Liu, C.; Zhao, Y.; Cai, X.; Xie, Y.; Wang, T.; Cheng, D.; Li, L.; Li, R.; Deng, Y.; Ding, H.; Lv, G.; Zhao, G.; Liu, L.; Zou, G.; Feng, M.; Sun, Q.; Yin, L.; Sheng, X. A Wireless, Implantable Optoelectrochemical Probe for Optogenetic Stimulation and Dopamine Detection. *Microsyst. Nanoeng.* **2020**, *6* (1), 64.
(25) Stuart, T.; Cai, L.; Burton, A.; Gutruf, P. Wireless and Battery-Free Platforms for Collection of Biosignals. *Biosens Bioelectron* **2021**, *178*, 113007.
(26) Burton, A.; Obaid, S. N.; Vázquez-Guardado, A.; Schmit, M. B.; Stuart, T.; Cai, L.; Chen, Z.; Kandela, I.; Haney, C. R.; Waters, E. A.; Cai, H.; Rogers, J. A.; Lu, L.; Gutruf, P. Wireless, Battery-Free Subdermally Implantable Photometry Systems for Chronic Recording of Neural Dynamics. *Proc. Natl. Acad. Sci. U. S. A.* **2020**, *117* (6), 2835.
(27) Ausra, J.; Munger, S. J.; Azami, A.; Burton, A.; Peralta, R.; Miller, J. E.; Gutruf, P. Wireless Battery Free Fully Implantable Multimodal Recording and Neuromodulation Tools for Songbirds. *Nat. Commun.* **2021**, *12* (1), 1968.
(28) Burton, A.; Won, S. M.; Sohrabi, A. K.; Stuart, T.; Amirhossein, A.; Kim, J. U.; Park, Y.; Gabros, A.; Rogers, J. A.; Vitale, F.; Richardson, A. G.; Gutruf, P. Wireless, Battery-Free, and Fully Implantable Electrical Neurostimulation in Freely Moving Rodents. *Microsyst Nanoeng* **2021**, *7* (1), 62.
(29) Zhao, X.; Cao, Y.; Liu, H.; Li, F.; You, B.; Zhou, X. Long Term High Frequency Stimulation of STN Increases Dopamine in the Corpus Striatum of Hemiparkinsonian Rhesus Monkey. *Brain Res.* **2009**, *1286*, 230−238.
(30) Gale, J. T.; Lee, K. H.; Amirnovin, R.; Roberts, D. W.; Williams, Z. M.; Blaha, C. D.; Eskandar, E. N. Electrical Stimulation-Evoked Dopamine Release in the Primate Striatum. *Stereotact Funct Neurosurg* **2013**, *91* (6), 355−363.
(31) Melchior, J. R.; Ferris, M. J.; Stuber, G. D.; Riddle, D. R.; Jones, S. R. Optogenetic versus Electrical Stimulation of Dopamine Terminals in the Nucleus Accumbens Reveals Local Modulation of Presynaptic Release. *J. Neurochem* **2015**, *134* (5), 833−844.
(32) Deisseroth, K. Optogenetics. *Nat. Methods* **2011**, *8* (1), 26−29.
(33) Pastrana, E. Optogenetics: Controlling Cell Function with Light. *Nat. Methods* **2011**, *8* (1), 24−25.
(34) Fenno, L.; Yizhar, O.; Deisseroth, K. The Development and Application of Optogenetics. *Annu. Rev. Neurosci.* **2011**, *34*, 389.
(35) Williams, J. C.; Entcheva, E. Optogenetic versus Electrical Stimulation of Human Cardiomyocytes: Modeling Insights. *Biophys. J.* **2015**, *108* (8), 1934−1945.
(36) Kim, M. H.; Yoon, H.; Choi, S. H.; Zhao, F.; Kim, J.; Song, K. D.; Lee, U. Miniaturized and Wireless Optical Neurotransmitter Sensor for Real-Time Monitoring of Dopamine in the Brain. *Sensors* **2016**, *16* (11), 1894.
(37) Zeng, Y.; Zhou, Y.; Kong, L.; Zhou, T.; Shi, G. A Novel Composite of SiO2-Coated Graphene Oxide and Molecularly Imprinted Polymers for Electrochemical Sensing Dopamine. *Biosens Bioelectron* **2013**, *45*, 25−33.
(38) Wang, W.; Xu, G.; Cui, X. T.; Sheng, G.; Luo, X. Enhanced Catalytic and Dopamine Sensing Properties of Electrochemically Reduced Conducting Polymer Nanocomposite Doped with Pure Graphene Oxide. *Biosens Bioelectron* **2014**, *58*, 153−156.
(39) Tsai, T. C.; Guo, C. X.; Han, H. Z.; Li, Y. T.; Huang, Y. Z.; Li, C. M.; Chen, J. J. J. Microelectrodes with Gold Nanoparticles and Self-Assembled Monolayers for in Vivo Recording of Striatal Dopamine. *Analyst* **2012**, *137* (12), 2813−2820.
(40) Cho, Y. H.; Park, Y.-G.; Kim, S.; Park, J.-U. 3D Electrodes for Bioelectronics. *Adv. Mater.* **2021**, *33* (47), 2005805.
(41) Li, Y.; Li, N.; de Oliveira, N.; Wang, S. Implantable Bioelectronics toward Long-Term Stability and Sustainability. *Matter* **2021**, *4* (4), 1125−1141.
(42) Shi, Y.; Liu, R.; He, L.; Feng, H.; Li, Y.; Li, Z. Recent Development of Implantable and Flexible Nerve Electrodes. *Smart Mater. Med.* **2020**, *1*, 131−147.
(43) Chen, Y.; Kim, Y.-S.; Tillman, B. W.; Yeo, W.-H.; Chun, Y. Advances in Materials for Recent Low-Profile Implantable Bioelectronics. *Materials* **2018**, *11* (4), 522.
(44) Dalu, A.; Blaydes, B. S.; Lomax, L. G.; Delclos, K. B. A Comparison of the Inflammatory Response to a Polydimethylsiloxane Implant in Male and Female Balb/c Mice. *Biomaterials* **2000**, *21* (19), 1947−1957.
(45) Zhang, H.; Gutruf, P.; Meacham, K.; Montana, M. C.; Zhao, X.; Chiarelli, A. M.; Vázquez-Guardado, A.; Norris, A.; Lu, L.; Guo, Q.; Xu, C.; Wu, Y.; Zhao, H.; Ning, X.; Bai, W.; Kandela, I.; Haney, C.; Chanda, D.; Gereau, R., IV; Rogers, J. Wireless, Battery-Free Optoelectronic Systems as Subdermal Implants for Local Tissue Oximetry. *Sci. Adv.* **2019**, *5* (3), eaaw0873.
(46) Zhang, Y.; Mickle, A. D.; Gutruf, P.; McIlvried, L. A.; Guo, H.; Wu, Y.; Golden, J. P.; Xue, Y.; Grajales-Reyes, J. G.; Wang, X.; Krishnan, S.; Xie, Y.; Peng, D.; Su, C.; Zhang, F.; Reeder, J.; Vogt, S.; Huang, Y.; Rogers, J.; Gereau, R., IV Battery-Free, Fully Implantable Optofluidic Cuff System for Wireless Optogenetic and Pharmacological Neuromodulation of Peripheral Nerves. *Sci. Adv.* **2019**, *5* (7), eaaw5296.
(47) Rogers, J. A.; Someya, T.; Huang, Y. Materials and Mechanics for Stretchable Electronics. *Science* **2010**, *327* (5973), 1603−1607.
(48) Hsu, Y.-Y.; Papakyrikos, C.; Liu, D.; Wang, X.; Raj, M.; Zhang, B.; Ghaffari, R. Design for Reliability of Multi-Layer Stretchable Interconnects. *Journal of Micromechanics and Microengineering* **2014**, *24* (9), No. 095014.
(49) Zen, J.-M.; Hsu, C.-T.; Hsu, Y.-L.; Sue, J.-W.; Conte, E. D. Voltammetric Peak Separation of Dopamine from Uric Acid in the Presence of Ascorbic Acid at Greater Than Ambient Solution Temperatures. *Anal. Chem.* **2004**, *76* (14), 4251−4255.
(50) Zestos, A. G.; Jacobs, C. B.; Trikantzopoulos, E.; Ross, A. E.; Venton, B. J. Polyethylenimine Carbon Nanotube Fiber Electrodes for Enhanced Detection of Neurotransmitters. *Anal. Chem.* **2014**, *86* (17), 8568−8575.
(51) Sheng, Z.-H.; Zheng, X.-Q.; Xu, J.-Y.; Bao, W.-J.; Wang, F.-B.; Xia, X.-H. Electrochemical Sensor Based on Nitrogen Doped Graphene: Simultaneous Determination of Ascorbic Acid. *Dopamine and Uric Acid. Biosens Bioelectron* **2012**, *34* (1), 125−131.
(52) Sajid, M.; Nazal, M. K.; Mansha, M.; Alsharaa, A.; Jillani, S. M. S.; Basheer, C. Chemically Modified Electrodes for Electrochemical Detection of Dopamine in the Presence of Uric Acid and Ascorbic Acid: A Review. *TrAC Trends in Analytical Chemistry* **2016**, *76*, 15−29.
(53) Dorta-Quiñones, C. I.; Huang, M.; Ruelas, J. C.; Delacruz, J.; Apsel, A. B.; Minch, B. A.; Lindau, M. A Bidirectional-Current CMOS Potentiostat for Fast-Scan Cyclic Voltammetry Detector Arrays. *IEEE Trans Biomed Circuits Syst* **2018**, *12* (4), 894−903.
(54) Deutch, A. Y.; Cameron, D. S. Pharmacological Characterization of Dopamine Systems in the Nucleus Accumbens Core and Shell. *Neuroscience* **1992**, *46* (1), 49−56.
(55) Zachek, M. K.; Takmakov, P.; Park, J.; Wightman, R. M.; McCarty, G. S. Simultaneous Monitoring of Dopamine Concentration at Spatially Different Brain Locations in Vivo. *Biosens Bioelectron* **2010**, *25* (5), 1179−1185.
(56) Versteeg, D. H. G.; Van der Gugten, J.; De Jong, W.; Palkovits, M. Regional Concentrations of Noradrenaline and Dopamine in Rat Brain. *Brain Res.* **1976**, *113* (3), 563−574.
(57) Kuczenski, R.; Segal, D. S.; Aizenstein, M. L. Amphetamine, Cocaine, and Fencamfamine: Relationship between Locomotor and Stereotypy Response Profiles and Caudate and Accumbens Dopamine Dynamics. *J. Neurosci.* **1991**, *11* (9), 2703.
(58) Wightman, R. M.; May, L. J.; Michael, A. C. Detection of Dopamine Dynamics in the Brain. *Anal. Chem.* **1988**, *60* (13), 769A−779A.
(59) Kilpatrick, M. R.; Rooney, M. B.; Michael, D. J.; Wightman, R. M. Extracellular Dopamine Dynamics in Rat Caudate−Putamen

https://doi.org/10.1021/acsnano.2c09475
ACS Nano 2023, 17, 561−574

during Experimenter-Delivered and Intracranial Self-Stimulation. *Neuroscience* **2000**, *96* (4), 697−706.
(60) Heien, M. L. A. v.; Khan, A. S.; Ariansen, J. L.; Cheer, J. F.; Phillips, P. E. M.; Wassum, K. M.; Wightman, R. M. Real-Time Measurement of Dopamine Fluctuations after Cocaine in the Brain of Behaving Rats. *Proc. Natl. Acad. Sci. U. S. A.* **2005**, *102* (29), 10023−10028.
(61) Phillips, P. E. M.; Robinson, D. L.; Stuber, G. D.; Carelli, R. M.; Wightman, R. M. Real-Time Measurements of Phasic Changes in Extracellular Dopamine Concentration in Freely Moving Rats by Fast-Scan Cyclic Voltammetry. *Drugs of Abuse*; Springer, 2003; pp 443−464.
(62) Johnson, M. A.; Rajan, V.; Miller, C. E.; Wightman, R. M. Dopamine Release Is Severely Compromised in the R6/2 Mouse Model of Huntington's Disease. *J. Neurochem* **2006**, *97* (3), 737−746.
(63) Kozler, P.; Marešová, D.; Pokorný, J. Study of Locomotion, Rearing and Grooming Activity after Single and/or Concomitant Lesions of Central and Peripheral Nervous System in Rats. *Neuroendocrinol. Lett.* **2017**, *38* (7), 495−505.
(64) Lin, J. C. A New IEEE Standard for Safety Levels with Respect to Human Exposure to Radio-Frequency Radiation. *IEEE Antennas Propag Mag* **2006**, *48* (1), 157−159.
(65) Ausra, J.; Wu, M.; Zhang, X.; Vázquez-Guardado, A.; Skelton, P.; Peralta, R.; Avila, R.; Murickan, T.; Haney, C. R.; Huang, Y.; Rogers, J. A.; Kozorovitskiy, Y.; Gutruf, P. Wireless, Battery-Free, Subdermally Implantable Platforms for Transcranial and Long-Range Optogenetics in Freely Moving Animals. *Proc. Natl. Acad. Sci. U. S. A.* **2021**, *118* (30), No. e2025775118.
(66) Mathon, D. S.; Vanderschuren, L. J. M. J.; Ramakers, G. M. J. Reduced Psychostimulant Effects on Dopamine Dynamics in the Nucleus Accumbens of μ-Opioid Receptor Knockout Mice. *Neuroscience* **2006**, *141* (4), 1679−1684.
(67) Spanagel, R.; Herz, A.; Shippenberg, T. S. The Effects of Opioid Peptides on Dopamine Release in the Nucleus Accumbens: An In Vivo Microdialysis Study. *J. Neurochem* **1990**, *55* (5), 1734−1740.
(68) Chefer, V. I.; Kieffer, B. L.; Shippenberg, T. S. Basal and Morphine-Evoked Dopaminergic Neurotransmission in the Nucleus Accumbens of MOR- and DOR-Knockout Mice. *European Journal of Neuroscience* **2003**, *18* (7), 1915−1922.
(69) Pontieri, F. E.; Tanda, G.; di Chiara, G. Intravenous Cocaine, Morphine, and Amphetamine Preferentially Increase Extracellular Dopamine in the "Shell" as Compared with the "Core" of the Rat Nucleus Accumbens. *Proc. Natl. Acad. Sci. U. S. A.* **1995**, *92* (26), 12304−12308.
(70) Pothos, E.; Rada, P.; Mark, G. P.; Hoebel, B. G. Dopamine Microdialysis in the Nucleus Accumbens during Acute and Chronic Morphine, Naloxone-Precipitated Withdrawal and Clonidine Treatment. *Brain Res.* **1991**, *566* (1), 348−350.
(71) Fox, M. E.; Rodeberg, N. T.; Wightman, R. M. Reciprocal Catecholamine Changes during Opiate Exposure and Withdrawal. *Neuropsychopharmacology* **2017**, *42* (3), 671−681.
(72) Arnsten, A. T.; Segal, D. S. Naloxone Alters Locomotion and Interaction with Environmental Stimuli. *Life Sci.* **1979**, *25* (12), 1035−1042.
(73) DeRossett, S. E.; Holtzman, S. G. Effects of Naloxone and Diprenorphine on Spontaneous Activity in Rats and Mice. *Pharmacol., Biochem. Behav.* **1982**, *17* (2), 347−351.
(74) Spanagel, R.; Almeida, O. F. X.; Shippenberg, T. S. Long Lasting Changes in Morphine-induced Mesolimbic Dopamine Release after Chronic Morphine Exposure. *Synapse* **1993**, *14* (3), 243−245.
(75) Marinelli, M.; Aouizerate, B.; Barrot, M.; le Moal, M.; Piazza, P. V. Dopamine-Dependent Responses to Morphine Depend on Glucocorticoid Receptors. *Proc. Natl. Acad. Sci. U. S. A.* **1998**, *95* (13), 7742−7747.
(76) Liu, X.; Liu, J. Biosensors and Sensors for Dopamine Detection. *VIEW* **2021**, *2* (1), 20200102.
(77) Copits, B. A.; Gowrishankar, R.; O'Neill, P. R.; Li, J.-N.; Girven, K. S.; Yoo, J. J.; Meshik, X.; Parker, K. E.; Spangler, S. M.; Elerding, A. J.; Brown, B. J.; Shirley, S. E.; Ma, K. K. L.; Vasquez, A. M.; Stander, M. C.; Kalyanaraman, V.; Vogt, S. K.; Samineni, V. K.; Patriarchi, T.; Tian, L.; Gautam, N.; Sunahara, R. K.; Gereau, R. W.; Bruchas, M. R. A Photoswitchable GPCR-Based Opsin for Presynaptic Inhibition. *Neuron.* **2021**, *109* (11), 1791−1809.
(78) Samineni, V. K.; Grajales-Reyes, J. G.; Grajales-Reyes, G. E.; Tycksen, E.; Copits, B. A.; Pedersen, C.; Ankudey, E. S.; Sackey, J. N.; Sewell, S. B.; Bruchas, M. R.; Gereau, R. W. Cellular, Circuit and Transcriptional Framework for Modulation of Itch in the Central Amygdala. *Elife* **2021**, *10*, No. e68130.
(79) Nath, T.; Mathis, A.; Chen, A. C.; Patel, A.; Bethge, M.; Mathis, M. W. Using DeepLabCut for 3D Markerless Pose Estimation across Species and Behaviors. *Nat. Protoc* **2019**, *14* (7), 2152−2176.

https://doi.org/10.1021/acsnano.2c09475
ACS Nano 2023, 17, 561−574